

Table 1 Intensities of the three components in the bright head of 3C273 corrected for Doppler beaming

Component	Distance from core (arc s)	Blue-shift	Observed flux density (mJy)	Intrinsic flux density (mJy)
1	22.1	1.2	450	216
2	21.4	3.4	1,500	13
3	20.4	4.0	450	3

We believe that other explanations that could be put forward are less probable than the following suggestion.

(4) The aspect angle may be modified by relativistic aberration. The angle θ_s , calculated above from the polarization, is that measured in the co-moving frame of the source. If component 2 is moving relativistically, aberration changes an inclination angle from θ_{jet} to θ_{obs} , given by $\sin \theta_{jet} = \eta \sin \theta_{obs}$, where η , the Doppler blue-shift, is given by $\eta = \gamma^{-1} (1 - \beta \cos \theta_{obs})^{-1}$. If we equate θ_{obs} with $\theta_0 = 12^\circ$ deduced from the superluminal motion and θ_{jet} with $\theta_s = 47^\circ$ deduced from the polarization, we obtain as the Doppler shift of component 2, $\eta \approx 3.4$. The Doppler shift measured in the frame co-moving with the quasar is larger by a factor $(1+z)_{QSO}$, that is, $\eta = 3.96$. Relative to the quasar the speed of component 2 is $\beta \approx 0.91$ and $\gamma \approx 2.4$. If component 2 is partially compressed (a thick sheet) then $\theta_s > 47^\circ$ and the values of β , γ and η given above should be regarded as lower limits.

We may apply these arguments to the precursor, component 1, which we suggest corresponds to the 'working surface' of the beam¹⁰ and moves with the speed of the bow shock. From ram pressure arguments² this speed must be sub-relativistic, in the range $0.02 < \beta < 0.3$. It follows that most of the deceleration occurs between component 2 and component 1. If the velocity of component 1 is $\beta = 0.2$, the Doppler shift $\eta = 1.22$, and the inclination angle in the emitting frame $\theta_{jet} \approx 14^\circ$. The polarization predicted for a Laing sheet would then be 2%, equal to that observed in component 1. Simulation models¹⁸ suggest that the working surface may be curved, in which case one may expect some polarization near the edge, but little in the centre of component 1. This description is entirely consistent with Fig. 1.

In this model, the relative intensities of the different components are altered by the Doppler beaming factor⁸ of $\eta^{3+\alpha}$. The Doppler shift of component 3 is not known, but the maximum value consistent with $\theta_0 = 12^\circ$ is 4.7, and if we assume a monotonic deceleration down the jet, η_3 must lie between 4.7 and $\eta_2 = 3.4$. We take $\eta_3 = 4$.

Applying a correction to the co-moving frame using Doppler shifts as above yields the intrinsic intensities given in Table 1, where it can be seen that the precursor is no longer a minor feature in front, but is intrinsically much the brightest component, as may be expected at the site of the greatest deceleration. Components 2 and 3 correspond to secondary features, which, if they were not amplified by beaming, would probably be classed as 'knots' similar to those found in many jets.

We thank A. R. Foley, R. J. Davis and R. A. Perley for data in advance of publication. C.F. thanks the SERC for a studentship.

Received 29 October 1984; accepted 30 January 1985.

- Schmidt, M. *Nature* **197**, 1040 (1963).
- Conway, R. G. *et al.* *Nature* **294**, 540-542 (1981).
- Perley, R. A. in *VLB and Compact Radio Sources* (eds Fanti, R., Kellerman, K. & Setti, G.) 153-156 (Reidel, Dordrecht, 1984).
- Schmidt, G. D., Peterson, B. M. & Beaver, E. A. *Astrophys. J. Lett.* **220**, L31-L37 (1978).
- Lelievre, G. *et al.* *Astr. Astrophys.* **138**, 49-56 (1984).
- Willingale, R. *Mon. Not. R. astr. Soc.* **194**, 359-364 (1981).
- Pearson, T. J. *et al.* *Nature* **290**, 365-368 (1981).
- Blandford, R. D. & Konigl, A. *Astrophys. J.* **232**, 34-48 (1979).
- Bridle, A. H. & Perley, R. A. *Rev. Astr. Astrophys.* **22**, 319-358 (1984).
- Begelman, M. C., Blandford, R. D. & Rees, M. J. *Rev. mod. Phys.* **56**, 255-351 (1984).
- Davies, J. G., Anderson, B. & Morison, I. *Nature* **288**, 64-66 (1980).
- Cornwell, T. J. & Wilkinson, P. N. *Mon. Not. R. astr. Soc.* **196**, 1067-1086 (1981).
- Conway, R. G. & Kronberg, P. P. *Mon. Not. R. astr. Soc.* **142**, 11-32 (1969).
- Conway, R. G. & Stannard, D. *Nature* **255**, 310-312 (1975).
- Laing, R. A. *Mon. Not. astr. Soc.* **193**, 439-449 (1980).
- Davis, R. J., Stannard, D. & Conway, R. G. *Mon. Not. R. astr. Soc.* **185**, 435-440 (1978).
- Laing, R. A. *Mon. Not. astr. Soc.* **195**, 261-324 (1981).
- Wilson, M. J. & Scheuer, P. A. G. *Mon. Not. R. astr. Soc.* **205**, 449-463 (1983).

Computer classification of sea beds by sonar

Z. Reut, N. G. Pace & M. J. P. Heaton

School of Physics, University of Bath, Bath BA2 7AY, UK

Direct sampling of the sea bed is not always feasible and can be unreliable because the samples obtained may not be representative. An alternative approach is to classify the superficial sea bed using the backscattered signal from side-scan sonars. The usual paper display contains less information than the signal creating it, because of its low dynamic range, and interpretation of sediment types is often difficult. There are also problems with statistical analysis of the signals¹. The usual methods of pattern recognition cannot resolve small-scale features in otherwise homogeneous regions² and, although the backscattering strength is a useful quantity, meaningful numerical values can be obtained only with a calibrated system³. To overcome these shortcomings we have now developed a spectral analysis method that is insensitive to system gain calibration. The method retrieves information from the signals that is well below the usual power spectrum point, thus effectively widening the system bandwidth, and can discriminate between the signals returned from six sea-bed types.

It can be shown theoretically that the scattered sound field depends on both roughness and hardness of the sediment/water interface⁴, but analytical expressions are unsuitable for most practical applications, not so much because of their complexity but because of the difficulty in quantifying roughness (statistically random corrugations) and hardness (mixed boundary conditions) of real sea beds. Although properties of scattered sound fields corresponding to an ensemble of sea-bed patches manifest only indirectly the combined effect of roughness and hardness on the incident sound field, they are nevertheless more suitable for our present semi-empirical approach. The shape of the probability distribution (of the scattered field intensity) does relate to the sea-bed roughness⁵, but is not so sensitive to its hardness.

We now consider a side-scan sonar transmitting a rectangular pulse of length T ($\gg T_0$) at carrier frequency $\omega_0 (= 2\pi/T_0)$. Received signal amplitude is proportional to the pressure of the sound field at the transducer. The received signal is a quasi-harmonic stochastic function of time ('reverberation') given by $a(t) \cos[\omega_0 t + \psi(t)]$, where $a(t)$ and $\psi(t)$ are the amplitude and the phase of the signal respectively, which are both assumed to be slowly varying functions of time in comparison with $\cos \omega_0 t$. Our method uses $a(t)$ only and yields numerical features that are invariant under the linear transformation of $a(t)$ and hence independent of the signal d.c. level and gain.

We denote by $a_i(t)$ the signal amplitude within the i th rectangular window ($i = 1, 2, \dots, n$) of a fixed time duration T_w ($\gg T$). The minimum value of the signal amplitude is set equal to zero so that $a_i(t) \geq 0$. The windows should have no temporal overlaps and can be taken from any number of pings. We further denote by $w(t)$ the time window function (other than rectangular) such that $w(t) = 0$ for $t < T_D$ and $t > T_D + T_w$, where T_D is the initial delay (measured from the instant of transmission). The resulting windowed signal can be written as $g_i(t) = w(t)a_i(t)$.

If the signal is digitized so that N samples are taken in each window with sampling interval Δt , we have $T_w = N\Delta t$. The Nyquist frequency is equal to $\pi/\Delta t$; if ω_B is the highest angular frequency of interest, the Nyquist sampling theorem implies $\Delta t \leq \pi/\omega_B$.

Performing the Fourier transform (operator \mathcal{F}) on the windowed amplitude $g_i(t)$ and taking the modulus squared of the resulting complex queffrequency amplitudes, the i th power spectrum is obtained as $P_i(\omega) = |\mathcal{F}\{g_i(t)\}|^2$. By averaging n power values at each frequency, we obtain the averaged power spectrum $\langle P(\omega) \rangle = n^{-1} \sum_{i=1}^n P_i(\omega)$, where it is assumed that the system

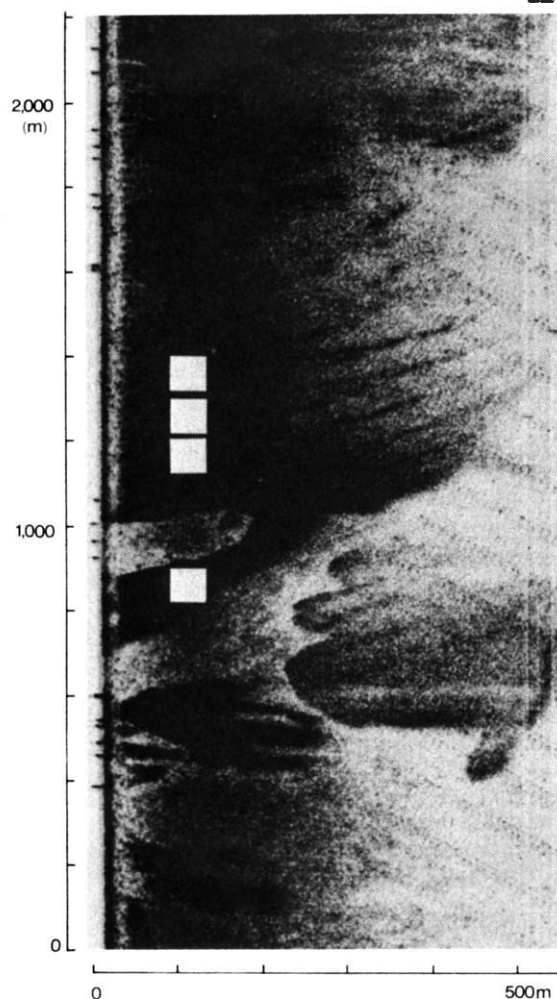


Fig. 1 Side-scan sonar paper record of sand and gravel sea-bed region. Blank squares indicate the approximate locations of four sample areas. The record width corresponds to 550 m range, the zero range being on the left-hand side. Sand and gravel appear as light and dark patches, respectively.

gain remains unaltered during the time taken to receive all n windows.

Performing the Fourier transform on the logarithm of the averaged power spectrum and taking the modulus squared of the resulting complex quantities, the power cepstrum (or simply 'cepstrum') is obtained $C(\tau) = |\mathcal{F}\{\log(P(\omega))\}|^2$, where the time-lag variable τ is called queffrequency. The cepstrum, applied to various seismic, speech analysis and machine vibration problems, appears to be more useful in certain cases^{6,7} than either the power spectrum or the auto-correlation function. However, we believe it has never been applied to side-scan sonar signals of 'reverberation' type not separating into 'echo' and 'noise'.

We define the power cepstrum integral (cumulative power cepstrum) by $I(\tau') = \int_0^{\tau'} C(\tau) d\tau / \int_0^{T_w} C(\tau) d\tau$, with the variable τ' in the range $\tau_0 \leq \tau' \leq T_w$, where $\tau_0 (\leq T)$ is a fixed interval.

We introduce two further parameters to characterize the power cepstrum integral, namely, the intercept and the slope at τ_0 given by $D_1 = 1 - I(\tau_0)$ and $D_2 = (d/d\tau')I(\tau')|_{\tau'=\tau_0}$, respectively, the cepstrum integral features, which both tend to zero when the cepstrum $C(\tau)$ contracts to the initial queffrequency range $0 \leq \tau \leq \tau_0$.

The side-scan sonar, used for data acquisition, is a standard medium range system operating at 48-kHz carrier frequency, 1-ms pulse length, 2-kHz nominal receiver bandwidth and the usual time-varied gain. The amplitude envelope is recorded on magnetic tape in analog form with 48-dB dynamic range. Hardware for data processing consists of an 8-bit A/D converter and a standard 32 K microcomputer with a dual disk drive. The amplitude envelope is digitized at a sufficiently high rate and

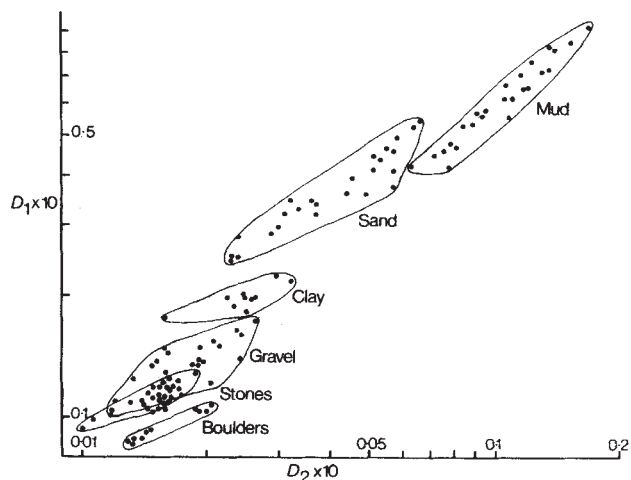


Fig. 2 Cepstrum integral features plane representation of all 120 sample areas. The boundaries to each sea-bed type are drawn by hand for clarity of display only. The time window $w(t)$ is chosen to be of the Hanning (cosine-squared) type. All Fourier transforms are performed according to the fast Fourier transform algorithm. The cepstrum is integrated numerically with a step equal to τ_0 and a straight line is interpolated through the first four points by the least-squares method in evaluating D_1 and D_2 . The gain independence of D_1 and D_2 as evaluated by our software has been tested numerically; change in gain by a factor of up to four causes deviations in D_1 and/or D_2 that are at most 5%. The numerical values of D_1 and D_2 for a given sea-bed type depend on the number of windows n , especially when n is small; both sequences (for D_1 and D_2) that correspond to $n = 1, 2, 4, 8, 16, 32$ converge relatively fast so that little can be gained by going to the values of $n > 32$.

integer values in the range 0–255 saved on disk for further processing. A typical side-scan sonar paper record is presented in Fig. 1.

All of our 120 sample areas are homogeneous as far as could be ascertained in real sea beds, are from regions familiar from previous surveys and are free from noise and interference. Based on records (like that in Fig. 1), as well as other knowledge of the regions, any one of the sample areas is assigned to only one of the six classes: mud, sand, clay, gravel, stones and boulders. The sample areas are geographically distributed as follows: mud (25 from the South Baltic Sea), sand (5 from Land's End, 10 from the Outer Hebrides and 10 from the western English Channel), clay (10 from the southern North Sea), gravel (10 from southern North Sea and 15 from western English Channel), stones (10 from South Baltic Sea and 15 from the Outer Hebrides) and boulders (10 from South Baltic Sea).

Table 1 contains the arithmetical mean and standard deviation of the two cepstrum integral features (D_1 and D_2 multiplied by 10) for the six sea-bed types. Numerical values for all 120 sample areas are presented graphically (log-log scale) in Fig 2; each sample area corresponds to a single point in the two-dimensional plot of D_1 against D_2 . Each sea-bed type corresponds to an area in (D_1, D_2) plane and the only overlap occurs between gravel and stones areas. Lower values of D_1 and D_2 generally

Table 1 Arithmetical mean and standard deviation of the cepstrum integral features for six sea-bed types

Sea-bed type	No. of sample areas	$D_1 \times 10$		$D_2 \times 10$	
		Mean	Dev.	Mean	Dev.
Mud	25	0.619	0.142	0.107	0.027
Sand	25	0.368	0.085	0.042	0.014
Clay	10	0.197	0.014	0.025	0.004
Gravel	25	0.135	0.018	0.018	0.004
Stones	25	0.111	0.007	0.015	0.002
Boulders	10	0.097	0.009	0.017	0.003

correspond to 'harder' sea-beds and the six sea-bed types span a factor of ~ 10 in the values of D_1 and D_2 .

Judging by our results, it seems certain that the cepstrum and its integral features must have an important role in the classification of sea beds. The dependence of the discriminatory ability of the method on pulse length and carrier frequency is presently being investigated especially with respect to the classification of non-homogeneous sea-bed regions (for example, sand with gravel).

We thank H. O. Berkay for stimulating discussions and the British Telecom Research Centre, Ipswich, UK, for support.

Received 11 October 1984; accepted 29 January 1985.

1. Ol'shevskii, V. V. *Characteristics of Sea Reverberation* (Consultants Bureau, New York, 1967).
2. Pace, N. G. & Dyer, C. M. *IEEE Trans. GE-17*, 52-56 (1979).
3. Wong, H.-K. & Chesterman, W. D. *J. acoust. Soc. Am.* **44**, 1713-1718 (1968).
4. Brekhovskikh, L. & Lysanov, Yu. *Fundamentals of Ocean Acoustics* (Springer, Berlin, 1982).
5. Stanton, T. K. *J. acoust. Soc. Am.* **75**, 809-818 (1984).
6. Bogert, B. P., Healey, M. J. R. & Tukey, J. W. in *Proc. Symp. Time Series Analysis* (ed. Rosenblatt, M.) 209-243 (Wiley, New York, 1963).
7. Noll, A. M. *J. acoust. Soc. Am.* **41**, 293-309 (1967).

Polarity reversal in the Solomon Islands arc

Patricia A. Cooper & Brian Taylor

Hawaii Institute of Geophysics, University of Hawaii,
2525 Correa Road, Honolulu, Hawaii 96822, USA

McKenzie¹ proposed that the direction of subduction beneath an island arc will reverse following arc-continent collision. Dewey and Bird² suggested that such an arc polarity reversal occurred in northern New Guinea; Johnson and Molnar³, however, proposed two alternative models of plate convergence that could explain the observed seismicity. We present here a spatial seismicity study of the Solomon Islands region which has revealed the existence of two juxtaposed Wadati-Benioff (W-B) zones of opposite polarity. Shallow and intermediate foci define a north-east-dipping W-B zone associated with active subduction along the New Britain and San Cristobal trenches and a south-west-dipping W-B zone associated with the inactive North Solomon trench (NST). These data provide the first direct seismic evidence of a reversal in subduction polarity at an island arc.

The Solomon Islands arc forms a linear double chain of islands north-east of the New Britain and San Cristobal trenches.

The arc-trench system is part of the convergent boundary between the westward-moving Pacific Plate and the northward-moving Indo-Australian Plate (Fig. 1). Arc volcanics provide evidence of convergence between the Pacific and Indo-Australian plates in this region since the early Eocene. The polarity of the subduction is thought to have varied and a number of different models of the tectonic evolution have been proposed⁴⁻⁷. Bathymetric and seismic reflection data indicate a relict subduction zone dipping south from the North Solomon and Vitiaz trenches^{8,9}. The abnormally thick lithosphere of the Ontong Java Plateau collided with the NST sometime during the Miocene, although the exact timing remains controversial^{14,7,9}. Following the collision, the arc polarity reversed and the present regime of north-east subduction at the New Britain, San Cristobal and Vanuatu trenches began by 10 Myr BP. The hiatus in island arc volcanism lasting from late-early to early-late Miocene observed throughout the Solomon Islands^{7,10} may be evidence of a temporary cessation of subduction during the polarity reversal.

Earthquake hypocentres, volcano locations and major tectonic features of the Solomon Islands region are illustrated in Fig. 2. Hypocentres covering the period 1 January 1964 to 30 June 1984 are taken from the International Seismological Centre (ISC) catalogue and include all events with body-wave magnitude ≥ 4.7 and recorded by more than 15 stations. Three primary features are evident from Fig. 2. First, the spatial density of earthquake foci changes along strike; shallow (< 70 km) and intermediate (70-300 km) activity is concentrated in two zones of greatest density under the northwestern and southeastern parts of the arc. Second, a zone of low-density shallow seismicity is associated with the active spreading system extending east across the Woodlark Basin. The low density of seismicity in the central Solomon Islands (from 156-159°E) coincides with the site of subduction of the young Woodlark Basin lithosphere. Third, diffuse shallow and intermediate seismicity is also observed north-east of New Georgia and Guadalcanal, extending to Santa Isabel and Malaita, which provides evidence of lithosphere previously subducted at the NST.

Four representative seismicity cross-sections located in Fig. 2 and one longitudinal section are shown in Fig. 3. The top of the subducted lithosphere is assumed to extend from the topographic trench axis downward along the upper limit of the concentrated seismicity. Both the dip and the depth-extent of the north-east-dipping W-B zone associated with subduction at the New Britain and San Cristobal trenches vary significantly along strike (Figs 2, 3). North of Bougainville, Fig. 3A shows a well-defined seismic zone dipping at an initially shallow angle, then steepening rapidly until becoming almost vertical below 100 km. Teleseismic activity is virtually absent in the overriding

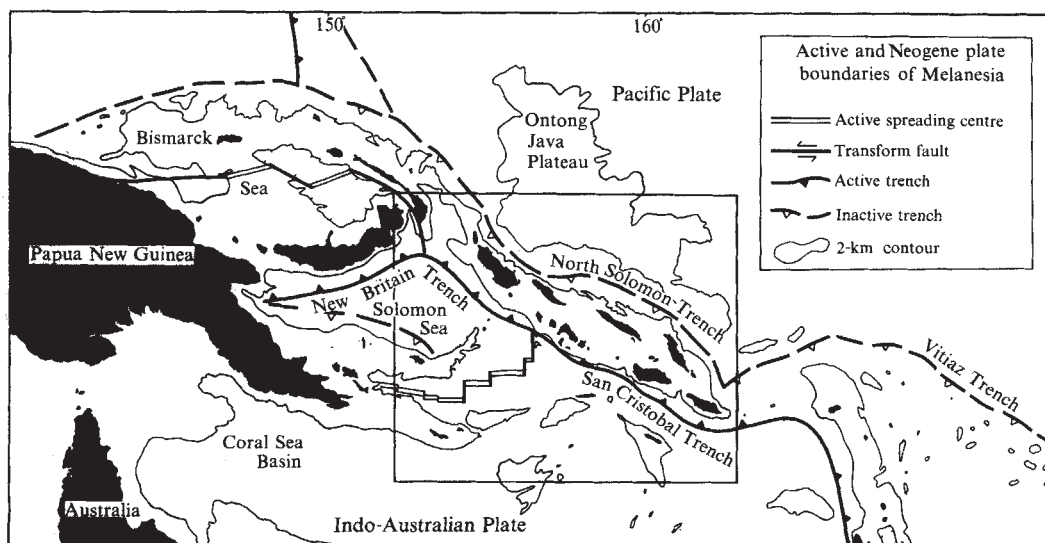


Fig. 1 Summary of active and Neogene plate boundaries of Melanesia (after ref. 19). Box shows location of Fig. 2.